Influence of Mg, Ag and Zn minor solute additions on the precipitation kinetics and strengthening of an Al-Cu-Li alloy

Eva Gumbmann, Frédéric de Geuser, Christophe Sigli, Alexis Deschamps

Influence of Mg, Ag and Zn minor solute additions on the precipitation kinetics and strengthening of an Al-Cu-Li alloy

Eva Gumbmann[1,2], Frédéric de Geuser[1], Christophe Sigli[2], Alexis Deschamps[1]

[1] Univ. Grenoble Alpes, CNRS, Grenoble INP*, SIMaP, F-38000 Grenoble, France

[2] Constellium Technology Center, CS 10027, 38341 Voreppe Cedex, France

Abstract

The influence of minor solute additions of Mg, Ag and Zn and their combinations on the precipitation kinetics and strengthening of an Al-Cu-Li alloy has been systematically investigated. Combining differential scanning calorimetry (DSC) and small-angle X-ray scattering (SAXS) provides information on how alloy chemistry changes the precipitation sequence, the precipitation kinetics in non – isothermal and in isothermal conditions, and the related strengthening. When adding Mg, the precipitation kinetics are strongly accelerated, which is shown to be related to the dominant formation of T_1 precipitates. When adding Ag and Zn together with Mg, further enhancement of precipitation kinetics is observed, without change of the precipitation sequence, probably due to a more efficient nucleation of T_1. The intrinsic strengthening potential of the T_1 phase is shown to be unchanged by the addition of Ag and Zn, and the higher strength reached in the alloys containing these additions is shown to be due to a higher precipitate volume fraction.

1. Introduction

Al-Cu-Li based alloys are currently the subject of intensive research for structural applications requiring a combination of high strength, low density, high fracture toughness and good corrosion resistance, these requirements being particularly relevant for aerospace applications [1]–[4]. Following the first generations of Al-Li alloys developed in the 1980s, the current developments concern alloys with lower Li content of the order of 1 wt%, which has helped improve some of the weak points of earlier developed alloys, such as limited long term microstructural stability [5]–[8].

* Institute of Engineering Univ. Grenoble Alpes

The mechanical properties of Al-Cu-Li alloys are controlled by the fine scale distribution of precipitate phases. In the base Al-Cu-Li system, the main phases that can form in practice during conventional heat treatments belong to the two binary systems Al-Cu (GPI and GPII zones and θ' phase, towards Al_2Cu composition [9]–[12]), Al-Li (δ' phases – Al_3Li [12], [13]), and to the ternary Al-Cu-Li system (T_1 phase Al_2CuLi [14]–[16]) ; other phases may form along higher temperature paths (θ, δ, T_2, σ, …). However, most Al-Cu-Li alloys have a more complex chemistry. Apart from solutes involved in dispersoids, which do not diffuse appreciably during precipitation heat treatments (Zr, Mn, …), combinations of Mg, Ag and / or Zn in fractions of % are frequently added, resulting in a potentially much wider variety of precipitating phases. Particularly, the importance of Mg-Cu phases (S phase and all its precursors such as clusters and GPB zones) has been clearly established [17]–[19].

The nucleation of the T_1 phase, usually considered to provide the highest strength in these alloys, forming thin plates of hexagonal structures lying on {111} matrix planes [20], [21] is quite challenging, especially at the relatively low ageing temperatures required to retain a good compromise of mechanical properties. It can be promoted by the introduction of strain prior to the artificial ageing treatment [9], [22]. Numerous studies have also shown that the precipitation of the T_1 phase could also be promoted by the addition of minor solute species, particularly Mg and Ag [23]–[27], [17], [13].

Ag addition alone does not alter the hardening potential to a great extent [25], [23], [28], [27], but the effect of Mg addition is much more pronounced [23], [26], [28], [29]. Mg addition promotes T_1 precipitation, to the expense of θ'' and θ' [19], [26], [28], [30], and the resulting distribution of T_1 phase (in the absence of pre-strain) has been shown to be finer [23]. In the presence of Mg, the addition of Ag has been shown to further improve the strengthening of Al-Cu-Li alloys [23], [28]. In parallel, Zn has been also used as a minor addition to Al-Cu-Li alloys, in combination with Mg [9], [31], [32].

In a recent article, we have studied the respective role of Mg, Ag and Zn additions on the precipitation sequence during different steps of artificial ageing at 155°C following a pre-deformation of an Al-3.5wt%Cu-0.9wt%Li alloy [19], using atomic resolution high angle annular dark field scanning transmission electron microscopy (HAADF-STEM). The main conclusions drawn from this study were as follows:

- The presence or absence of Mg profoundly changes the precipitation path. In the absence of Mg, at early ageing times the microstructure contained GPI zones that later developed into θ' precipitates, curved along the dislocations where they nucleated. Only a limited number of T_1 precipitates were observed. In the presence of Mg, however, precursor Mg-Cu phases were found at dislocations very early along the heat treatment that further developed in GPB

zones and S phase along with a high density of T_1 precipitates that dominated the microstructure. A threshold Mg concentration of the order of 0.1 at% was found necessary to activate this change of precipitation path [30].

- Ag was found at the interface between T_1 precipitates and the matrix as early during the heat treatment as the T_1 precipitates were observed, confirming the observations of [18]. However, its presence did not change qualitatively the precipitate microstructure after artificial ageing. Similarly, Zn was found to be present inside the precipitates, most probably substituting for Cu atoms. Like that of Ag, the addition of Zn did not change qualitatively the precipitate microstructure.

Thus, a better level of understanding of the precipitation sequence has been reached with respect to the effect of minor solute additions of Mg, Ag and Zn. However, little is known about the influence of these profound changes of precipitation sequence with minor alloying additions, on the precipitation kinetics and on the associated evolution of strength. Moreover, Mg, Ag and Zn may be used together or in various combinations, and the role of the combination of these has not yet been established. In Al-Cu-Li based alloys, maximizing the intragranular precipitation kinetics is of paramount importance because at long ageing times, grain boundary precipitation contributes to a reduction in ductility and toughness [33]. As a consequence, the T8 condition of these alloys is generally chosen in a slightly underaged state at the beginning of the hardness plateau where a good compromise between intra-granular strength and minimal grain boundary precipitation can be achieved.

In this context, this paper will present a thorough evaluation of precipitation kinetics, in both isothermal and non-isothermal conditions, as well as the related strengthening kinetics, in a series of alloys with systematic combinations of minor solute additions (Mg, Ag, Zn). The precipitation kinetics will be investigated by combining small-angle X-ray scattering (SAXS) and differential scanning calorimetry (DSC), supported by transmission electron microscopy (TEM).

2. Materials and methods

The alloys of the study all share the same concentration of 3.5%Cu and 0.9%Li (all compositions are in wt%) as major alloying elements. Based on this solute content (named subsequently the base alloy), a number of alloys containing different combination of Mg, Ag and Zn in small proportions were prepared. The alloy compositions are given in Table 1. The heat treatment consisted of a solution heat treatment at 505 °C for 30 minutes, followed by a water quench. A plastic pre-deformation of 4% was added after water quench followed by 3 days of natural aging. Artificial aging started with a ramp heating from room temperature (RT) up to 155 °C with 20 °C/hour and isothermal aging was then performed at 155 °C in an oil bath.

For hardness measurements, the samples were water quenched from 155 °C for different aging times and tested on a fully automatic Buehler Tukon™1102 instrument. The applied load was 500gr and indentation time 10 seconds. For each ageing time and alloy, the average value is calculated on 60 measurements.

Small-Angle X-ray Scattering (SAXS) measurements were performed both on a laboratory rotating anode (Rigaku MicroMax-OO7 HF, Cu K_α source) and at the European Synchrotron Radiation Facility (ESRF). For aluminium alloys the optimal sample thickness at the energy of the Cu Kα the energy (8.048 keV) is around 75 µm. The data were acquired by a DECTRIS Pilatus 300K X-ray Detector, which performs single-photon counting on each pixel. The same energy was provided at the ESRF. Due to a higher flux, it is possible to measure with shorter acquisition times compared to the laboratory setup. This was taken advantage of for the continuous heating experiments. A CCD camera was used for detection in this case. The precipitates present in this system are strongly anisotropic, which results in a signal on the detector which is the combination of streaks representative of the precipitates lying close to an edge-on geometry. However, the particular grain texture present in our alloys did some averaging of this intensity, which prevented the analysis of individual streaks such as performed in [34], [35] to extract the morphology of the precipitates. Instead, a radial averaging of the data was made, which is equivalent to making the hypothesis that grains of all orientations are within the illuminated volume. This hypothesis was sufficiently robust to extract quantitatively morphological parameters such as the precipitate thickness (see appendix), but the integrated intensity, which is usually related to the precipitate volume fraction in a rather simple way [36], is very sensitive to the detailed texture of the zone covered by the X-ray beam. As a consequence, although the relative variation of intensity could be safely interpreted during an in-situ heating experiment because the local texture does not change, converting this relative intensity to an absolute volume fraction measurement required the use of an independent measurement, which was made using Differential Scanning Calorimetry.

DSC measurements were performed with a Perkin Elmer Pyris Diamond apparatus. DSC samples had a weight between 30-50 mg. The ramp heating was either 50 °C/min or 200 °C/min. The scanned temperature interval goes from 25 to 550 °C. Baseline corrections were done, by adjusting temperature intervals between 50 to 100 °C and above 500 °C to zero heat flow by using a polynomial function of 3rd order. These temperature intervals were chosen, because precipitation is expected to occur above this lower temperature boundary and all present phases should have been dissolved above 500 °C [37].

Conventional TEM was performed at the SIMaP laboratory on a JEOL 3010 instrument, operated at 300 kV. With the aperture diameter available on this instrument, the $<112>_{Al}$ orientation was favourable to form good dark field images (with the aperture centred around the $\{110\}_{Al}$ forbidden

reflexion) given the larger distance between matrix diffraction spots as compared to the <110>$_{Al}$ zone axis. TEM samples were polished with a double jet Tenupol in an electrolyte consisting of 70 % CH_4O and 30 % HNO_3, cooled down to below -20 °C.

3. Results

3.1. Hardness

Figure 1 presents the evolution of hardness over aging time at 155°C for the different alloys. It can be observed on these curves that the standard deviation of the measurements (60 indents per condition) varies during the heat treatment. As shown in [38], the relatively wide distribution of hardness in these alloys is related to the relative inhomogeneity of plastic strain induced by the pre-deformation from grain to grain, inducing a local variation in precipitation kinetics. The time scale is plotted in logarithmic scale with respect to the time of the 'End of Ramp' ('EoR') condition, and the conditions prior to 'EoR' are placed arbitrarily on this time scale. After water quench, the hardness of all alloys is very similar and lies around 70 – 75 HV. Two groups of alloys can be distinguished after pre-deformation and subsequent natural aging. The first group contains Mg and hardness increases up to 95 HV by pre-deformation. The second group, with no Mg additions, shows hardness values around 10 HV below Mg containing alloys after pre-deformation. Three days of natural aging ('NA') amplifies the hardness difference between Mg containing and Mg-free alloys which is then around 20 HV. All Mg containing alloys follow the same hardness evolution after pre-deformation and natural aging. No additional effect of Ag or Zn is observed. Subsequently, a ramp heating up to 155 °C is performed. The hardness slightly decreases at the end of ramp condition compared to the hardness values after natural ageing. The difference between Mg containing and Mg-free alloys is still 20 HV. Upon further artificial aging at 155 °C a hardness increase within 1 hour is observed, which then accelerates until reaching a hardness plateau. Again, the main difference during artificial ageing is visible between Mg containing and Mg-free alloys, whose strengthening kinetics is both slower and reaching a lower plateau value. After 4 hours of artificial aging, a small effect of Ag in Mg containing alloys becomes also visible. The hardness of alloys containing Ag or Zn additions increases faster. Maximum hardness is reached for different aging times, depending on the presence of minor alloying elements. The highest hardness is measured for the Base + Mg0.3Ag and the Base + Mg0.1AgZn alloys (173 HV) and the lowest hardness is measured in the Base alloy. In addition, these alloys need different aging periods in order to reach the plateau hardness. Table 2 summarizes the maximum hardness value and the corresponding aging time for all alloys. The ageing condition corresponding to this time will subsequently be named 'stabilized condition'.

3.2. Microstructure in the precipitated state

The effect of Mg, Ag and Zn on the precipitate microstructure in these alloys was described in [19]. As recalled in the introduction, it was shown that Mg essentially affects the precipitation path: in the presence of Mg the microstructure at the hardness plateau is dominated by the T_1 phase, whereas in the absence of Mg, it is dominated by the θ' with only a low number density of T_1.

To analyse the detailed effect of all combinations of minor alloying elements on the distribution and diameter of T_1 precipitates, conventional dark field TEM imaging was performed in the 'stabilized' condition for each alloy. These observations were performed along the <112> matrix zone axis, where only one variant of T_1 precipitates (out of four) is imaged. The shape of T_1 precipitates was assumed to be disc-like, and the measured projected length on TEM was assimilated to the precipitate diameter. For each alloy, the diameter of 100 – 200 precipitates was measured. The obtained distributions are shown in supplementary material. They represent only the diameter of the T_1 precipitates, which do not necessarily represent the major phase in all alloys (namely not in the Mg-free alloys).

The shape of the diameter distributions of T_1 precipitates is quite similar for the two Mg-free alloys. With increasing minor alloying content, it appears that the size distribution expands towards higher diameter values. For example, in the Base alloy most of the diameters range from 30 to 50 nm. In the Base + MgZn0.1Ag and Base + Mg0.3Ag the range of diameters is much wider with values from 30 to 80 nm. Only small differences in the average measured diameters, shown in Table 2, are observed between the different alloys. The smallest average diameter is found for the Base alloy (42 nm) and Base + 0.3Ag (43 nm). The diameter increase, when Mg is added, is very small (45 nm). Further additions of alloying elements, such as Ag and Zn, lead to slightly larger diameters. However, no clear trend with respect to the minor additions could be found. The Base + MgZn (48 nm) and Base + Mg0.3Ag (45 nm) alloys reach similar diameters, which are very close to the diameter of the Base alloy. The highest values are obtained for the Base + Mg0.1AgZn (55 nm) and Base + Mg0.1Ag (60 nm) alloys. The half width (at half maximum) of the distribution for all alloys is comprised between 19 and 25 nm.

The dark field images shown in Figure 2 are taken at the same magnification for each alloy. They reveal qualitatively that the T_1 number density in Mg-free alloys is much lower than in Mg containing alloys, and is similar within the latter group of alloys.

In Ref. [19] it was shown that in the absence of Mg, precipitation at peak strength is dominated by the θ' phase. This is illustrated in Figure 3(a) where the 'stabilized' condition of the Base alloy is imaged in dark field along <001> zone axis, where two out of the three variants of θ' are visible. Qualitatively, the density of θ' appears to be high. In comparison, the Base + Mg0.1Ag alloy,

representative for Mg containing alloys, and imaged in the same conditions, shows a much lower number density of θ' (Figure 3(b)). In addition, the contrast in the TEM micrograph exhibits a plate-like phase which is not edge-on in the <001> zone axis. They are most likely T_1 phases, which are inclined to the zone axis. This confirms the fact that in the Base alloy, precipitation of θ' plays an important role, whereas it is of smaller importance in the presence of Mg.

3.3. Precipitation kinetics during isothermal ageing

The kinetics of precipitation during isothermal ageing at 155°C (preceded by the heating ramp) has been characterised in all alloys using in-situ small-angle X-ray scattering. Figure 4 shows 2D scattering patterns in the stabilized condition for all studied alloys, and the corresponding radially averaged intensity vs. scattering vector plots, compared to the scattering signal in the naturally aged state and at the end of the ramp. The naturally aged state shows a scattering signal at large angles, representative of small clusters. In the end of ramp condition, this signal has mostly disappeared, reflecting the cluster dissolution, and scattering intensity at smaller angles experiences a moderate increase, reflecting the nucleation of the first precursor phases at the dislocations.

The SAXS images of the stabilized condition all show the presence of streaks, which are representative of a signal dominated by the scattering by platelet particles. This is confirmed by the radially averaged curves, which show an extended q^{-2} behaviour representative of platelet particles, before tending towards a q^{-4} behaviour at large angles.

The volume fraction and the average thickness of the precipitates is extracted from the fit of the intensity as described in the Appendix. This allows further analysis and comparison of the different alloys with each other. However, the scattering images of Figure 4 show a large number of streaks, whose angular distribution appears close to random. This is because the alloys of the present study present a partially recrystallized microstructure, in contrast to former studies e.g. on the 2198 alloy of strongly unrecrystallized microstructure [12], [37]. The recorded intensity depends on the relative fraction of the platelets which are oriented to give rise to the streaks (close to edge-on conditions, depending on the scattering vector considered, see [34]). The local texture probed by the beam varies from one alloy to another but is constant during an in-situ experiment, so that it is possible to represent the fitted volume fraction from the model in relative units for a given alloy at any time during the heat treatment. In order to compare the alloys together, this volume fraction in arbitrary units was normalized based on two assumptions.

First, the 'EoR' condition was considered not to contain any precipitates. The value of the volume fraction at this point was therefore set to 0. The observations of [19] show that this assumption is not strictly true for the local microstructure at the dislocations, however averaged on the material's volume the volume fraction of precipitates in this condition was considered to be negligible,

consistent with the SAXS signal observed in the EOR samples in Figure 4. Secondly, after aging for 50 hours it was assumed based on the hardness measurements that a constant volume fraction was reached in all alloys, which was defined as fully precipitated state at this temperature and set to 1. It must be stressed that the measurements of platelet thickness, however, are not affected by this normalization procedure, as they solely depend on the relative evolution of intensity with scattering vector.

Figures 5a and 5b show the evolution of relative volume fraction and platelet thickness for the same group of alloys as for the hardness curves in Figure 1. The graphs start all at the beginning of the 155°C isothermal heat treatment (at the 'EoR' condition). The volume fraction rises quite rapidly during artificial aging at 155 °C. Similarly to hardness measurements, Mg containing and Mg-free alloys can be clearly distinguished. A difference is seen in the initial slope of the volume fraction evolution, which is steeper for Mg containing alloys. A plateau of precipitate volume fraction for Mg containing alloys is reached after 15 hours for Base + Mg0.3Ag, 18 hours for Base + Mg0.1Ag and 22 hours for Base + Mg, respectively. Mg containing alloys show intensities slightly above 1 for aging times of around 20 hrs. This is due to the fact that normalisation to 1 was made at 50 hours, which does not correspond to maximum intensity. A decrease in intensity during ageing seems at first sight counter-intuitive. However, it can be explained by a change in contrast conditions due to subtle changes in the composition of the different layers constituting the T_1 precipitate. As shown in [15], small changes of the chemical composition of the T_1-phase can result in large changes of the contrast conditions and thereby change the global intensity measured in SAXS, because of the opposite contrast of Li and Cu with respect to Al in X-rays. In the absence of Mg the precipitation process takes much longer and maximum precipitation is achieved only after 50 hours at 155 °C. The addition of Ag in the ternary AlCuLi (Base) alloy slightly enhances the overall precipitation kinetics.

In the presence of Mg, the addition of Zn, Ag or (Zn & Ag) affects the precipitate volume fraction in a very similar way. All of these three alloys reach the plateau of maximum precipitation after around 18 hours. Only the Base + Mg alloy, which does not contain any additional alloying elements, shows slightly slower kinetics.

Additionally, the evolution of the average thickness of the precipitates can be extracted from the obtained SAXS data and results are illustrated in Figure 5b. The obtained thicknesses for all alloys lie between 1.1 and 1.3 nm for the investigated time range at 155°C. It appears that the addition of both Mg and Ag is most effective to avoid thickening. At this point, it is important to recall that the results present the average thickness of all scattering objects, based on a discrete size distribution, which takes into account the discrete nature of the possible T_1 thickness [39], [40]. However, a moderate increase of the average thickness such as observed in Figure 5b can be attributed either to an increased proportion of T_1 platelets with additional layers, or to the thickening of other phases which

do not form with the same geometry, like θ'. The additions of only Zn or Zn and Ag likewise result in a constant thickness, which does not evolve appreciably over time but which is slightly higher than for the Base + Mg0.3Ag alloy. Slight differences in the average thickness are observed to be in the order of 0.2 nm and are considered to be negligible.

The thickness of T_1 is closely connected to heat treatment temperature. Aging at 155 °C of a pre-deformed sample results mainly in precipitation of single layered T_1 [18], [37] ; Dorin et al. observed only thickening when changing the heat treatment temperature to 190 °C [37]. It thus may be concluded that in the investigated conditions, precipitated T_1 phases are mostly single-layered for all alloys studied, in good agreement with the constant hardness plateau observed in section 3.1, since thickening of T_1 precipitates results in a sharp loss in hardening [35].

3.4. Precipitation kinetics during non-isothermal ageing

The previous section has highlighted the effect of minor alloying elements on precipitation kinetics, with a good agreement between hardness measurements and SAXS data. However, subtle differences in the precipitation sequence induced by the addition of minor solutes cannot be resolved by these experiments only, and require complementary measurements by differential scanning calorimetry (DSC). On two alloys, DSC measurements were combined with in-situ SAXS-experiments realised in the same experimental conditions to relate the visualization of the signature of the precipitate evolution on SAXS images to the DSC signal, based on the methodology proposed by Dorin et al. [37].

Figure 6 shows the normalized heat flux for the Base alloy initially in the naturally aged condition and heated at 50 °C/min. Characteristic points are indicated in the DSC graph and the corresponding snapshots from SAXS measurements in the same conditions are displayed below in Figure 6. In Figure 6a no precipitates or clusters are present. The signal slowly rises in Figure 6b at around 260 °C and its intensity becomes stronger in Figure 6c. The relatively isotropic distribution of the signal suggests that both T_1 and θ' are present when compared to the scattering from Mg containing alloys (Figure 4), because these two phases do not form on the same habit planes and therefore give rise to streaks at different angles. The signal increases for temperatures up to 317 °C (Figure 6d – e) which is the temperature of maximum precipitation rate identified on the DSC thermogram. Further heating shows the shortening of the scattering streaks, which are related to thickening of the existing phases (Figure 6f and g). At 452 °C, which lies clearly on the endothermic side of the DSC graph, complete dissolution has occurred. Based on these observations, the broad exothermic peak in DSC can therefore be attributed to combined precipitation of T_1 and θ'.

A similar experiment coupling DSC and SAXS measurements has been carried out for the Base + Mg alloy. This experiment is very similar to that carried out by Dorin et al. [37] on the AA2198 alloy, and the results can be found in the supplementary material. As can be seen in Figure 7 where the DSC curves for all alloys are reported, the non-isothermal precipitation kinetics in the Mg containing alloy is markedly different from that of the Mg-free alloy. From the comparison with SAXS images, the small endothermic peaks in the temperature range below 230°C are attributed to dissolution of clusters formed during natural aging. Comparing our SAXS images to those recorded in unrecrystallized rolled alloys [12], [34], [37] our results strongly support that most of the streaks present during the main exothermic event in DSC correspond to precipitates lying in the {111} planes, with no evidence for significant presence of platelets lying on the {100} planes. This observation further confirms the attribution of this main sharp DSC peak to the precipitation of the T_1 phase, with the second DSC exothermic peak at 340°C being attributed to the secondary precipitation related to thickening of T_1 precipitates.

The normalized DSC signals are compared for all alloys in Figure 7. Similarly to the observations made for isothermal ageing, the largest difference is found between Mg containing and Mg-free alloys. Based on the combined SAXS and DSC analysis, we can deduce that when precipitation is dominated by T_1 (in the presence of Mg), precipitation occurs much more rapidly as illustrated by the much narrower precipitation peak.

In the absence of Mg, the addition of Ag is observed to significantly change the precipitation kinetics in these non-isothermal conditions, contrarily to what has been observed in isothermal ageing. Namely, the exothermic peak in the Base + 0.3Ag alloy is much narrower, and at lower temperature, as compared to that of the Base alloy. This indicates that precipitation kinetics are faster in the presence of Ag.

In the presence of Mg, all DSC curves are qualitatively similar, confirming that the addition of Ag and Zn are of second order importance. However, the effect of alloying elements affects both the area of the main exothermic peak, which is representative of the volume fraction of precipitates, and the peak temperature, which can be qualitatively related to precipitation kinetics. Figure 7 shows that the addition of 0.1 wt % and 0.3 wt % Ag results in a larger peak area, i.e., an increased volume fraction for T_1. The kinetics is slightly enhanced as well by the addition of Ag, since the peak temperature is lower as compared to the Base + Mg alloy. The addition of Zn has a similar effect as the addition of Ag, and the DSC signal of the Base + MgZn0.1Ag alloy is almost identical to that of the Base + Mg0.3Ag alloy. In contrast, of all Mg containing alloys, the Base + Mg alloy possesses the slowest precipitation kinetics and lowest volume fraction of T_1.

3.5. Quantification of the precipitate volume fraction and relation to strengthening

Until now, we have evidenced an effect of minor solute additions on the precipitation kinetics. However, a more complete understanding requires a determination of the precipitate volume fraction in absolute units. For T_1 precipitates, Dorin et. al. [37] established a relationship between the normalised enthalpy measured by DSC and the precipitate volume fraction measured by TEM. The normalized enthalpy for a given microstructural state (e.g. the stabilized condition) is measured by subjecting this state to a DSC scan and by integrating the DSC signal up to the solvus temperature. We applied this relationship to DSC experiments carried out on the stabilized condition of all different alloys. As assumed by Dorin et al [37], T_1 is the main precipitating phase in the AA2198 alloy, which contains Mg and Ag in addition to the main solutes Cu and Li. The integral of the DSC curve which describes the thermal events $Q_i(T)$ varies for different aging conditions and is proportional to the volume fraction of precipitates f_V present in the sample at the beginning of the DSC scan. The normalised enthalpy is defined as:

$$\Delta H = \frac{1}{\beta}\int_{100°C}^{520°C} Q_i(T)dT \propto f_V \qquad \textbf{Equation 1}$$

β is the heating ramp of the experiment, set to 200°C to maximise the DSC signal and minimise the possible phase transformations (apart from T_1 dissolution) occurring during the experiment. The indicated integration boundaries are the same as in [37], assuming that below 100 °C no thermal events are happening and above 520 °C all former precipitated phases have dissolved. The T8 condition of AA2198 contains a precipitation volume fraction of 2.6 % and measures a normalized enthalpy of 13.9 J/g in DSC analysis, respectively [37]. In the present study, the alloys differed by minor alloying elements. We used the aging times to reach the stabilized condition as presented in Table 2 for the different alloys. Only Mg containing alloys were taken into account, since an important assumption of the procedure is that the microstructure contains mainly T_1 precipitates.
Figure 8 shows the DSC curves for the different Mg containing alloys in the stabilized condition. Most of the thermal events are endothermic and related to dissolution.

Table 3 summarizes the area, calculated by integration of the heat flow with time and the corresponding volume fraction calculated from the relationship given by Dorin et al. [37]. It shows that the highest volume fraction is obtained for the Base + Mg0.1AgZn and Base + Mg0.3Ag alloys.
Figure 9 shows the precipitation kinetics curve obtained from SAXS measurements, and now converted to volume fraction. All curves in Figure 9 show a similar precipitation behaviour, however differences in volume fraction are obtained. The Base + Mg alloy reaches a plateau at a volume fraction of 3.3 %. The addition of 0.1 wt% Ag results throughout the ageing treatment in a higher

volume fraction and reaches a maximum volume fraction of 3.8 %. An even higher T_1 volume fraction is obtained for the Base + Mg0.3Ag alloy, which reaches a value of up to 4%. In the presence of Zn, the maximum volume fraction is 4 %. The addition of both Zn and Ag shows the highest volume fraction of 4.35 %.

The calibrated volume fraction can now be related to the hardness of the different alloys. Figure 10 shows the relation between the calibrated volume fraction and the hardness, measured during the 155°C heat treatment. It is seen that for all alloys a linear relationship is obtained. From Figure 10, it is seen that with higher Ag or Zn concentration a higher T_1 volume fraction, and correspondingly a higher hardness is obtained. The highest effect in terms of both precipitate volume fraction and strengthening is the combined addition of Zn and Ag.

4. Discussion

The former described results will now be discussed together, with the help of the microstructure information at the atomic scale shown in [19] to elucidate, when possible, the effect of minor alloying elements on the precipitation kinetics, and on the related strengthening of the Al-Cu-Li alloys under study. The effect of Mg on precipitation kinetics will be first discussed, followed by the effect of adding Ag in the absence of Mg and last by the influence of the addition of Zn and/or Ag in the presence of Mg.

4.1. The effect of Mg addition on precipitation kinetics and related strengthening

In-situ small angle X-ray scattering reveals that the precipitate volume fraction for Mg containing alloys increases faster during artificial ageing as compared to Mg-free alloys. Similar behaviour was observed for hardness measurements, where Mg containing alloys exhibit faster hardening kinetics and higher end hardness values. DSC measurements of naturally aged alloys showed that Mg-free alloys present a different precipitation sequence compared to Mg containing alloys, and that this different precipitation sequence results in a precipitation kinetics spanning over a much wider temperature range. These observations confirm the microstructural observations of [19]. It was shown that Mg-free alloys contained a high number density of θ’ and a low number density of T_1 precipitates, whereas the Mg containing alloys showed a high number density of T_1 and a low number density of θ’.

Therefore, the observed influence of Mg on precipitation is two-fold: -i- the addition of Mg changes the dominating precipitating phase, namely T_1 is the main precipitate in the presence of Mg, and θ’ is the main precipitate in the absence of Mg; and -ii- in the presence of Mg, the overall precipitation

kinetics are observed to be much faster. These two observations might have a common origin, or could result from different effects.

The first observation has been discussed in detail based on the early stage microstructure in [19]. *In the absence of Mg*, Cu containing GP zones are observed very early on the dislocations ('EoR' condition). In the 'nucleation' condition, corresponding to the time when the first precipitates are detected by macroscopic methods (SAXS), these GP zones have already evolved to θ', which are inclined to follow the shape of the curved dislocations. In the 'stabilized' condition the microstructure is then dominated by these precipitates. T_1 precipitates are also observed, however in low quantity, and seem also to have nucleated on dislocations. The low density of T_1 precipitates in the Mg-free alloy with respect to the θ' phase seems therefore related to a kinetic competition between the formation of these two phases on the dislocations. The formation of T_1 on a dislocation exempt from precursors requires the dissociation of this dislocation [22], which in aluminium is difficult because of the high stacking fault energy. Consequently, it is kinetically unfavourable compared to θ' phase formation, which evolves from the pre-existing GP zones.

When Mg is present, microstructure observations strongly suggest that the dislocations are completely covered with Mg-Cu precursors [18], [19], which prevent the formation of θ'. If the formation of θ' is suppressed, and the further growth of Mg containing phases is made difficult by the shortage of Mg, it follows that the nucleation of T_1 should be favoured. Since it is observed to happen quickly and with a high number density, one can conclude that the Mg-Cu rich precursors on dislocations have a structure that helps the formation of T_1 nuclei.

Thus, as observed both by in-situ SAXS, DSC and hardness, in the presence of Mg, T_1 (together with the limited number of θ') precipitates faster than the concomitant precipitation of T_1 and θ' in the absence of Mg. This difference in precipitation kinetics is at first sight counter-intuitive, since in both microstructures one finds the same precipitates (although in different proportions), namely θ' and T_1, competing for the same limiting solute (Cu), and their observed sizes are comparable.

A first possible explanation of this difference in precipitation kinetics may be the difference in precipitate number density. A system with a higher density of nuclei will precipitate faster because the diffusion distance to be covered by solutes during the growth process is smaller. [19] showed measurements of the surface fraction of T_1 precipitates by TEM. The surface fraction for T_1 precipitates in Mg containing alloys is approximately twice that of Mg-free alloys. However, the latter also contain a high density of θ' and the final size of T_1 precipitates is similar in both alloy families, which indicates that the total number density of particles is of the same order. Thus, there is no indication that the two alloy families present a very large difference in total precipitate number density, which would explain the accelerated precipitation kinetics in the presence of Mg.

A second possible explanation is that the kinetics are faster in Mg containing alloys because the precipitates (namely, T_1) nucleates earlier. The condition 'nucleation' was defined as the ageing time for which first streaks appear in SAXS measurements. Interestingly, for both Mg containing and Mg-free alloys the 'nucleation' condition was found to be 1.5 hours at 155°C. This confirms the microscopic observations that in the 'nucleation' condition a high number density of precipitates are present both in Mg containing and Mg-free alloys, even though they are not of the same type. This rules out an effect of the nucleation time.

Another explanation of the difference in kinetics could be that the growth rate of T_1 and θ' precipitates are different in the Mg-containing and in the Mg-free alloys. Then, when the microstructure is dominated by T_1 the overall kinetics would be faster, and when it is dominated by θ' it would be slower. The interface structure of the T_1 phase with the matrix on the habit plane has almost no misfit strain, which favours the growth of this phase by reducing the build-up of elastic stresses. In contrast the growth of θ' is more complex. θ' is known to be semi-coherent [41], [42]. As shown in [19], it does not grow straight in these pre-deformed alloys but follows the dislocations, which impose a complex structure arrangement. Moreover, in straight sections it is surrounded by an ordered Al_3Li phase at its interface with the matrix. It is difficult to state if this layer forms together with the growth of θ' or subsequently at room temperature, but in the first case it would make the access of Cu solute atoms at the growing interphase more difficult. These different levels of complexity of the growth of θ' could lead to a slower growth rate than that of T_1. However, this interpretation alone also leads to some inconsistencies. Namely, the T_1 precipitates observed in the Mg-free alloy in the stabilized condition should then be much larger than in the Mg containing alloy, because of their lower number density and their longer ageing time as compared to the Mg containing alloys. The only explanation that could reconcile our observations with this interpretation is that most of the T_1 observed in the Mg-free alloy appear subsequently to the θ' precipitates, because they nucleate at sites associated with a higher activation energy, so that their growth is impeded by the existing θ', both in terms of available solute (soft impingement) and by hard geometrical impingement. This is compatible with the facts that in the 'nucleation' condition a well-developed θ' microstructure can already be observed in the Mg-free alloy. Then, if this interpretation is correct, the overall observed kinetics (by non-isothermal DSC or by SAXS) would be controlled by the majority phase, whereas the minority phase grows at its pace and takes the remaining volume available in the microstructure, which is plenty in the case of platelet precipitates.

A last mechanism that we can consider is related to a possible direct influence of Mg on the growth rate of T_1. Since T_1 precipitation is possible in both Mg containing and Mg-free alloys, an effect on the kinetics could be the difference in growth rate of the T_1 diameter. The presence of Mg on the T_1

interfaces and its incorporation inside the precipitates as observed by [18] may affect the interfacial energy and hence influence the lengthening rate.

To summarise, there is now strong evidence that the presence or absence of the Mg containing precursors is the major factor that explains the difference in precipitation path, namely the competition between T_1 and θ', in between the Mg containing and Mg-free alloys. The situation is more complex for the difference in precipitation kinetics. We have reviewed several possible effects, which are likely to have a combined influence: the presence of Mg promotes a moderately higher number density of precipitates earlier in the ageing process, T_1 grows faster than θ' but nucleates after this phase in Mg-free alloys, and possibly the presence of Mg accelerates the growth rate of T_1.

Effect on hardness

The hardness increase correlates well with the increase in precipitate volume fraction as it has been determined by SAXS measurements. In the as-quenched condition the hardness for all alloys is very similar, but after pre-deformation and even more visibly after 3 days of natural aging, the hardness of Mg containing alloys increases to higher values. The difference in hardness at this stage can be attributed to the formation of precursors on dislocations in Mg containing alloys. Cu-Mg-vacancy co-clustering has been observed in Al-Cu-Mg alloys and is associated to the rapid hardening phenomenon [43], [44]. The hardness difference between Mg containing and Mg-free alloys remains constant even during the ramp heating, after which hardness values have slightly decreased compared to the naturally aged condition. The nearly constant hardness difference of Mg containing and Mg-free alloys can be attributed to the Cu-Mg containing precursors, which are present in the microstructure throughout the precipitation sequence.

During further aging, the hardness starts to increase at similar aging times at 155°C, which is attributed to precipitation of mainly T_1, and θ' and T_1, in Mg containing and Mg-free alloys, respectively. The increase in hardening kinetics is in very good agreement with precipitation kinetics obtained by SAXS measurements. Hardness increases from the onset of nucleation and longer artificial aging times are necessary for Mg-free alloys in order to achieve maximum hardness, corresponding to the observed slower precipitation kinetics.

The strengthening contributions for θ', T_1 and precursors are certainly different. T_1 strengthens due to a shearing mechanism [35], [45], and it has been shown that in order to achieve a high strength with T_1 precipitates it was desirable to achieve a large T_1 diameter while retaining the 1 unit cell thickness [35], [46]. θ' on the other hand, is much more difficult to shear, and is generally considered to be non shearable. It has been shown by Da Costa Teixeira et al. [47] that its strengthening contribution in an Al-Cu alloy could be described by the dimension of the precipitate-free channels between the grown platelets. The comparison between the strengthening potential from a

microstructure dominated by T_1 precipitates (in the Mg containing alloy) and from a microstructure dominated by θ' (in the Mg-free alloys) is however no easy task, because it involves many factors: a different equilibrium volume fraction (Cu being the limiting solute, Al_2CuLi provides a higher volume fraction than Al_2Cu), a different strengthening mechanism, different habit planes ({100} is intrinsically more effective as compared to {111} [48]), different geometric characteristics, and a complex addition of the strengthening contributions in case of the simultaneous presence of the two phases. Actually it has been shown that a similar strength could be achieved by both types of particles [9]. In addition, when Mg-free alloys achieve highest hardness after 50 hours the differences with Mg containing alloys are still around 20 HV, the same as after natural aging. The S' phase and GPB zones still present at this stage must contribute to the strength, and thus it cannot be ruled out that the difference in peak strength between the two alloy families is mainly controlled by the presence of these phases. Therefore, the fact that we observe a higher peak strength when T_1 dominates the microstructure is consistent with the usually accepted fact that this phase is the most potent strengthener for AlCuLi alloys, but it is no easy task to demonstrate by what mechanism this effect can be rationalised.

4.2. Influence of Ag addition in the Mg-free alloy

The addition of Ag to the Base alloy results only in a small effect on hardness and precipitation kinetics obtained by SAXS measurements in isothermal conditions at 155°C, although the dark field electron micrographs in the stabilized condition suggest that in the presence of Ag the proportion of T_1 is somewhat enhanced. However, a much larger effect is observed by DSC in non-isothermal conditions: although the Base and Base + 0.3Ag alloys show a similar shape of the precipitation peak, which indicates the presence of similar phases, the addition of 0.3Ag shifts the peak to lower temperatures and make it narrower, which is associated to enhanced precipitation kinetics. The difference between isothermal and non-isothermal experiments means that the effect of Ag is temperature dependent. Increased hardness values due to Ag addition to AlCuLi alloys were identified by Zheng et al. [25]. Huang and Zheng [28] showed that in the presence of Ag in an AlCuLi alloy, the GP zone formation was suppressed and consequently the θ' precipitate density was lower. However, this effect was cancelled when pre-deformation was introduced prior to artificial aging [25], which might explain similar hardness values for the Base and Base + 0.3Ag alloys in the present study.

In summary, the influence of Ag on precipitation in the Base alloy is to favour the T_1 phase in competition with the θ' phase. Although this does not result in measurable changes of precipitation and strengthening kinetics at 155°C, this effect is observed to be temperature dependent and more

effective at the higher temperatures probed by DSC scanning. This effect may be related to the influence of Ag on the stacking fault energy of aluminium and its role on T_1 nucleation in Mg-free alloys, or to the effect of Ag on limiting the nucleation of θ', or to a combination of both effects.

4.3. Influence of the addition of Zn and Ag in the presence of Mg

Effect on kinetics

The effect of different additions of Ag, Zn or (Ag and Zn) on precipitation kinetics is of second order as compared to the major role played by Mg. However, an enhancement of precipitation kinetics is identified compared to the Base + Mg alloy, which can make an important difference to the compromise of mechanical properties since these alloys generally benefit from a slightly under-aged condition to avoid a loss of toughness associated with grain boundary precipitation [33], [49]. In contrast to the effect of an addition of Ag to the Base alloy seen above, the moderate influence on kinetics is observed both in isothermal and non-isothermal conditions.

As observed in [18], [19] Ag segregation at the T_1/matrix interface is observed from the earliest observation of this phase, namely in the 'EoR' and in 'nucleation' conditions. No EDX measurements on T_1 precipitates in the Zn containing alloys could be performed for such early aging times, but we can reasonably assume from the microstructure at later ageing times that Zn segregations are also present at this stage. Both elements probably lower the activation energy for T_1 nucleation, which indirectly promotes a faster overall precipitation kinetics. Ag being located specifically at the interface may have a larger effect on the interfacial energy, whereas Zn, which seems to substitute more generally to Cu, may influence more the volume free energy of T_1. In addition, by substituting to Cu in T_1, part of the effect of Zn may be simply related to increasing the alloy supersaturation (total amount of solute), without favouring the formation of θ' which is not expected to contain Zn.

Effect on hardness

Ag and Zn additions result in slightly higher hardness values and enhanced hardening kinetics compared to the Base + Mg alloy. These effects are moderate but significant. After natural aging and ramp heating, no differences in hardness are observed and the effect of Zn and Ag on hardening kinetics is observed only during subsequent artificial aging.

The additional strengthening observed when Ag and Zn are added could be related to a higher volume fraction of induced precipitation, or to a higher strengthening efficiency of a same precipitate volume fraction. Both effects could of course also combine.

As seen in figure 10, a linear relationship between hardness and precipitate volume fraction is observed, similarly to that observed by Dorin et al. [35] and by Rodgers and Prangnell [46] and

expected from the strengthening model developed by Dorin et al. when the T_1 thickness remains that of one unit cell. Within experimental uncertainty, it is not possible to discriminate between the different slopes as function of addition of Ag, Zn or the combination of both. These results therefore rule out that the observed higher strength in Ag and Zn containing alloys would be due to an increased strengthening efficiency of the T_1 precipitates in the presence of Ag and/or Zn. Instead, the higher hardness in these latter alloys is due to a higher overall precipitate volume fraction as confirmed by the DSC measurements. Consequently, all points representative of the highest hardness in figure 10 correspond as well to the highest volume fraction and belong to the Ag and/or Zn added alloys.

As shown by Dorin [37] on a similar alloy, the volume fraction obtained in the 'stabilized' condition at 155°C is quite far from the equilibrium value, because the lack of T_1 thickening at this temperature does not enable all the solute trapped in between the precipitates to reach them. Consequently, differences in volume fraction in such ageing conditions do not have to be related to changes of equilibrium volume fraction (which is probably only possible for Zn, see above), but can also be due to changes in the efficiency of accessing the solute during the precipitation process, particularly by promoting a more efficient nucleation.

Neglecting the effect of the precipitate size distribution, the precipitate volume fraction f_v depends on the precipitate number density N_V, thickness t and diameter D as follows:

$$f_V \propto \frac{N_V \, \pi \, t \, D^2}{4} \qquad \textbf{Equation 2}$$

For the heat treatment at 155°C, it is reasonable to assume constant thickness for the precipitates. An increased precipitate volume fraction can thus be influenced by two factors: an increase in number density of precipitates or an increase in the precipitate diameter. An increased number density is possible if the nucleation rate is enhanced, which could be related to the effect of Ag and Zn on the interface or volume free energy of the T_1 phase as discussed above, but could not be confirmed by our TEM observations due to the uncertainties of sample thickness for the conventional dark field observations.

As seen in Equation 2, the influence of the diameter on the volume fraction is quite important. The measured diameters (see table 2) in the present study showed variations between 45 to 60 nm between alloys, but no clear trend could be observed with respect to minor alloying elements. Probably the variability of diameters in the microstructures is quite high, depending on the local dislocation density in the grains observed in TEM. It has been shown in [38] that the variability of the hardness distribution in these alloys was related to the variability of the dislocation density introduced during pre-deformation from one grain to another.

In summary, the effect of Ag, Zn and combined (Ag and Zn) affects the volume fraction of T_1 precipitates, which is the main precipitating phase in the presence of Mg. The increase of volume fraction is well correlated to the increase in hardness. The highest hardness and volume fraction of T_1 were found in the Base + Mg0.3Ag and the Base + Mg0.1AgZn alloys. It is likely that the presence of Ag and Zn provides a more efficient nucleation of the T_1 phase and thus helps reaching a higher volume fraction, through combined effects of decreased interfacial energy (Ag), increased supersaturation and decreased volume free energy (Zn). Density Functional Theory (DFT) calculations are needed to provide more insight on the preferential location of these solutes in the T_1 structure embedded in Al matrix, and on their effect on the energetics of the system.

5. Conclusion

The effect of minor alloying elements (Mg, Ag, Zn and combinations of them) on precipitation kinetics and on the related hardness in an Al-Cu-Li alloy has been determined. Combining complementary experimental techniques makes it possible to draw some conclusions on the respective roles of the different solute additions, applicable for the particular case studied here, namely a low Li content and precipitation in a pre-deformed material.

- Mg is the most important addition to Al-Cu-Li. Its presence changes the precipitation sequence to mainly T_1 phase as compared to mainly θ’ in an Mg-free alloy. A change in precipitation kinetics is associated to this change in precipitation path, which appears to be mainly related to a faster precipitation kinetics for T_1 precipitates as compared to θ’ phase constrained by the dislocations. The hardening kinetics follow well the precipitation kinetics, and the final increased hardness in the presence of Mg may be related to a more efficient strengthening by T_1, or to the presence of S’ and GPB zones at the dislocations.
- An addition of Ag, when no Mg is present in the alloy, leads to a higher proportion of T_1 precipitates, possibly due to an Ag effect on the trapping of vacancies, which reduces the GP zone formation and consequently θ’ formation. The observed higher hardness in the presence of Ag can therefore be attributed to a higher proportion of T_1. The effect of Ag on precipitation kinetics is strongly temperature-dependent, with an enhanced effect in non-isothermal conditions as compared to isothermal ageing at 155°C.
- When adding Ag, Zn or their combination to a Mg containing alloy, the microstructure and precipitation sequence are qualitatively not modified. However, these additions result in an enhanced precipitation kinetics, a higher precipitate volume fraction in isothermal conditions

and a higher strength. The presence of Ag at the T_1/matrix interface and of Zn within the precipitate seem to play a role in favouring the nucleation of this phase and help reaching a higher volume fraction. However they do not seem to play a direct role in the strengthening efficiency of T_1, and the additional strength in the Ag,Zn added alloys is mainly controlled by the larger precipitate volume fraction.

Acknowledgements

This work was performed within the framework of the Centre of Excellence of Multifunctional Architectured Materials "CEMAM" n° ANR-10-LABX-44-01. Pauline Poncet is thanked for conducting hardness measurements. The technical staff of beamline BM02/D2AM of the European Synchrotron Radiation Facility (ESRF) is thanked for technical support. We would also like to thank Dr. Williams Lefebvre for his support with TEM experiments and fruitful discussion.

Appendix: extraction of average precipitate thickness from radially averaged SAXS data

According to [50], the radially averaged SAXS intensity given by an assembly of platelets of thickness *t*, diameter *D* and volume fraction f_v can be written (when *D*>>t and *qD*>>1):

$$I_1(q,t) = \Delta\rho^2 f_v \frac{2\pi t}{q^2}\left(\frac{\sin\frac{qt}{2}}{\frac{qt}{2}}\right)^2 \qquad \textbf{Equation A1}$$

Where $\Delta\rho^2$ is the electronic density contrast between matrix and precipitates. The interesting feature of eq. A1 is that it is independent of *D*. The oscillating sine term is expected to give strong oscillations, in particular a zero intensity at $q = \frac{2\pi}{t}$. While the T_1 precipitates are known to form mostly as single unit-cell thickness [37], even a moderate dispersion in the thickness distribution (in this case, the presence of a few 2-layers, 3-layers or more precipitates) is likely to damp the presence of these zeros in the function. The discrete nature of the possible thicknesses of the precipitates does not allow the use of usual continuous size dispersion functions (such as Gaussian or log-normal). Instead we use a discrete distribution based on a Poisson law. It is based on the assumption that the multi-layer nature of the precipitates is governed by a Poisson probability. The precipitates thickness is that of a single unit-cell plus a Poisson distribution of additional layers. The probability of obtaining the thickness $t_n = t_1 + n \cdot \delta t$ is given by the usual Poisson law:

$$P(n,\lambda) = \frac{\lambda^k}{n!}e^{-\lambda} \qquad \textbf{Equation A2}$$

In this case λ is the average number of additional layers, so that the average precipitate thickness can be written:

$$t =< t >= t_1 + \lambda \cdot \delta t \qquad \textbf{Equation A3}$$

t_1 is the thickness of a single unit cell T_1 precipitate, while δt is the thickness of one additional layer. While we might expect these two values to be equal to about 4 d_{111} of Al (which is the unit cell parameter of the T_1 phase), the single layer precipitates also include some rearrangement at the interface and their effective thickness is expected to be somewhat larger. We estimated $t_1$to be about *9.5 Å* and we used 4 d_{111} distances (about *9.3 Å*) for δt.

The SAXS intensity of the precipitates is then given by the sum of the contribution of each class of precipitates. After noticing that the number density of each class is given by $n_v P_n$, with n_v the overall number density, and assuming a constant cross section area for each precipitate, the total intensity reads

$$I(q,t) = \Delta\rho^2 f_v \frac{4\pi}{q^4 t} \sum_{n=0}^{\infty} P_n \left(\sin\frac{q t_n}{2}\right)^2 \qquad \textbf{Equation A4}$$

In practice, the sum only needs to run up to the value for which P_n is still significant. In our cases, the contribution of precipitates with *n* superior to 8 was always negligible. This model has 2 parameters, *t* and f_v (or rather, its product with $\Delta\rho^2$), the unit cell and single layer thicknesses being considered as constants. As previously discussed, the volume fraction considered here cannot be absolutely calibrated because i) it is extremely dependent on the local texture and ii) it cannot be separated from the electronic density contrast which may not be constant throughout the experiment or from an alloy to another. We will only consider relative variations and attempt an absolute calibration from external information, namely DSC experiments.

In addition to the precipitates signal, we will consider a background signal which corresponds to the Laue incoherent scattering of the disordered matrix (which gives a constant contribution) and the Porod behavior of large objects (e.g. dispersoids) giving rise to a contribution to intensity at low q (proportional to q^{-4}).

6. References

[1] T. Warner, Recently-developed aluminium solutions for areospace applications, *Mat. Sci. Forum* 519–521 (2006) 1271–1278.

[2] P. Lequeu, K. P. Smith, A. Danielou, Aluminum-Copper-Lithium Alloy 2050 Developed for Medium to Thick Plate, *J. Mater. Eng. Perform.*,19 (2010) 841–847.

[3] R. J. Rioja, J. Liu, The Evolution of Al-Li Base Products for Aerospace and Space Applications

Metall. Mater. Trans. 43A (2012) 3325–3337.

[4] N. Eswara Prasad, A. A. Gokhale, R. J. H. Wanhill, *Aluminium-Lithium Alloys*. Elsevier, Oxford, 2014.

[5] B. Noble, S. J. Harris, S. Katsikis, K. Dinsdale, Low temperature thermal stability of quaternary Al-Li-Cu-Mg alloys, *Mat. Sci. Forum* 519–521 (2006) 209–214.

[6] D. Ortiz, J. Brown, M. Abdelshehid, P. Deleon, R. Dalton, L. Mendez, J. Soltero, M. Pereira, M. Hahn, E. Lee, J. Ogren, R. Clark, J. Foyos, O. S. Es-Said, The effects of prolonged thermal exposure on the mechanical properties and fracture toughness of C458 aluminum-lithium alloy, *Eng. Fail. Anal.*, 13 (2006) 170–180.

[7] S. Katsikis, B. Noble, S. J. Harris, Microstructural stability during low temperature exposure of alloys within the Al-Li-Cu-Mg system, *Mat. Sci. Eng. A* 485 (2008) 613–620.

[8] A. Deschamps, M. Garcia, J. Chevy, B. Davo, F. De Geuser, Influence of Mg and Li content on the microstructure evolution of AlCuLi alloys during long-term ageing, *Acta Mater.* 122, (2017) 32–46.

[9] B. M. Gable, A. W. Zhu, A. A. Csontos, E. A. J. Starke, The role of plastic deformation on the competitive microstructural evolution and mechanical properties of a novel Al-Cu-Li-X alloy, *J. Light Met.* 1 (2001) 1–14.

[10] R. Yoshimura, T. J. Konno, E. Abe, K. Hiraga, Transmission electron microscopy in the early stages of precipitates in aged Al-Li-Cu alloys, *Acta Mater.* 51 (2003) 2891–2903.

[11] R. Yoshimura, T. J. Konno, E. Abe, K. Hiraga, Transmission electron microscopy study of the evolution of precipitates in aged Al–Li–Cu alloys: the θ′ and T1 phases, *Acta Mater.* 51 (2003) 4251–4266.

[12] B. Decreus, A. Deschamps, F. De Geuser, P. Donnadieu, C. Sigli, M. Weyland, The influence of Cu/Li ratio on precipitation in Al-Cu-Li-x alloys, *Acta Mater.* 61 (2013) 2207–2218.

[13] A. K. Khan, J. S. Robinson, Effect of silver on precipitation response of Al-Li-Cu-Mg alloys RID D-1730-2009, *Mater. Sci. Technol.* 24 (2008) 1369–1377.

[14] S. Van Smaalen, A. Meetsma, J. L. D. Boer, P. M. Bronsveld, Refinement of the crystal structure of hexagonal Al2CuLi, *J. of Solid State Chem.* 85 (1990) 293–298.

[15] P. Donnadieu*, Y. Shao, F. De Geuser, G. A. Botton*, S. Lazar, M. Cheynet, M. de Boissieu, A. Deschamps, Atomic structure of T-1 precipitates in Al-Li-Cu alloys revisited with HAADF-STEM imaging and small-angle X-ray scattering, *Acta Mater.* 59 (2011) 462–472.

[16] C. Dwyer, M. Weyland, L. Y. Chang, B. C. Muddle, Combined electron beam imaging and ab initio modeling of T(1) precipitates in Al-Li-Cu alloys, *Appl. Phys. Lett.* 98 (2011) 201909.

[17] B. Gault, F. De Geuser, L. Bourgeois, B. M. Gable, S. P. Ringer, B. C. Muddle, Atom probe tomography and transmission electron microscopy characterisation of precipitation in an Al–Cu–Li–

Mg–Ag alloy, *Ultramicroscopy* 111 (2011) 683–689.

[18] V. Araullo-Peters, B. Gault, F. de Geuser, A. Deschamps, J. M. Cairney, Microstructural evolution during ageing of Al–Cu–Li–x alloys, *Acta Mater.* 66 (2014) 199–208.

[19] E. Gumbmann, W. Lefebvre, F. De Geuser, C. Sigli, A. Deschamps, The effect of minor solute additions on the precipitation path of an AlCuLi alloy, *Acta Mater.* 115 (2016) 104–114.

[20] P. Sainfort, B. Dubost, Coprecipitation hardening in Al-Li-Cu-Mg alloys, *Journal de Physique*, C3, N°9 (1987) 407–413.

[21] J. C. Huang, A. J. Ardell, Addition rules and the contribution of δ' precipitates to strenghtening of aged Al-Li-Cu alloys, *Acta Metall.* 36 (1988) 2998–3006.

[22] W. A. Cassada, G. J. Shiflet, E. A. J. Starke, The effect of plastic deformation on Al2CuLi (T1) precipitation, *Metall. Trans.* 22A (1991) 299–306.

[23] G. Itoh, Q. Cui, M. Kanno, Effects of a small addition of magnesium and silver on the precipitation of T1 phase in an Al—4%Cu—1.1%Li—0.2%Zr alloy, *Mat. Sci. Eng. A* 211 (1996) 128–137.

[24] J. R. Pickens, F. H. Heubaum, T. J. Langan, L. S. Kramer, Al-(4.5-6.3)Cu-1.3Li-0.4Ag-0.4Mg-0.14Zr weldalite 049, in *Proceedings of the 5th International Al-Li conference, 1989, Williamsburg, VA, USA* (1989), vol. 3, pp. 1397–1414.

[25] Z. Zheng, S. Liang, H. Xu, C. Tan, D. Yun, Effect of 0.5-Percent Silver on the Age-Hardening Behavior of an Al-Li-Cu-Mg-Zr Alloy, *J. Mater. Sci. Lett.* 12 (1993) 1111–1113.

[26] D. L. Gilmore, E. A. J. Starke, Trace elements effects on precipitation processes and mechanical properties in an Al-Cu-Li alloy, *Metall. and Mater. Trans.* 28A (1997) 1399–1415.

[27] M. Murayama, K. Hono, Role of Ag and Mg on precipitation of T1 phase in an Al-Cu-Li-Mg-Ag alloy, *Scripta Mater.* 44 (2001) 701–706.

[28] B. P. Huang, Z. Q. Zheng, Independent and combined roles of trace Mg and Ag additions in properties precipitation process and precipitation kinetics of Al–Cu–Li–(Mg)–(Ag)–Zr–Ti alloys, *Acta Mater.* 46 (1998) 4381–4393.

[29] S. Hirosawa, T. Sato, A. Kamio, "Effects of Mg addition on the kinetics of low-temperature precipitation in Al-Li-Cu-Ag-Zr alloys, *Mater. Sci. Eng. A* 242 (1998) 195–201.

[30] E. Gumbmann, F. De Geuser, A. Deschamps, W. Lefebvre, F. Robaut, C. Sigli, A combinatorial approach for studying the effect of Mg concentration on precipitation in an Al–Cu–Li alloy, *Scripta Mater.* 110 (2016) 44–47.

[31] R. Kilmer, G. Stoner, Effect of Zn Additions on Precipitation During Aging of Alloy-8090, *Scripta Metall. Mater.* 25 (1991) 243–248.

[32] M. J.-F. Guinel, N. Brodusch, G. Sha, M. A. Shandiz, H. Demers, M. Trudeau, S. P. Ringer, R. Gauvin, Microscopy and microanalysis of complex nanosized strengthening precipitates in new

generation commercial Al-Cu-Li alloys, *J. Microsc.* 255 (2014) 128–137.

[33] B. Decreus, A. Deschamps, P. Donnadieu, J. C. Ehrstroem, On the role of microstructure in governing fracture behavior of an aluminum-copper-lithium alloy, *Mater. Sci. Eng. A* 586 (2013) 418–427.

[34] F. De Geuser, F. Bley, A. Deschamps, A new method for evaluating the size of plate-like precipitates by small-angle scattering, *J. Appl. Crystallogr.* 45 (2012) 1208–1218.

[35] T. Dorin, A. Deschamps, F. De Geuser, C. Sigli, Quantification and modelling of the microstructure/strength relationship by tailoring the morphological parameters of the T1 phase in an Al–Cu–Li alloy, *Acta Mater.* 75 (2014) 134–146.

[36] F. De Geuser, A. Deschamps, Precipitate characterisation in metallic systems by small-angle X-ray or neutron scattering, *C. R. Phys.* 13 (2012) 246–256.

[37] T. Dorin, A. Deschamps, F. De Geuser, W. Lefebvre, C. Sigli, Quantitative description of the T1 formation kinetics in an Al–Cu–Li alloy using differential scanning calorimetry, small-angle X-ray scattering and transmission electron microscopy, *Phil. Mag.* 94 (2014) 1012–1030.

[38] T. Dorin, A. Deschamps, F. De Geuser, F. Robaut, Impact of grain microstructure on the heterogeneity of precipitation strengthening in an Al-Li-Cu alloy, *Mater. Sci. Eng. A* 627 (2015) 51–55.

[39] W. A. Cassada, G. J. Shiflet, E. A. J. Starke, Mechanism of Al2CuLi (T1) nucleation and growth, *Metall. Trans.* 22A (1991) 287–297.

[40] J. M. Howe, J. Lee, A. K. Vasudévan, Structure and deformation behaviour of T1 precipitate plates in an Al-2Li-1Cu alloy, *Metall. Trans.* 19A (1988) 2911–2920.

[41] J. M. Silcock, T. J. Heal, H. K. Hardy, Structural Ageing Characteristics of Binary Aluminium-Copper Alloys, *J. Inst. Metals* 82 (1953-1954), 239-248.

[42] L. Bourgeois, C. Dwyer, M. Weyland, J.-F. Nie, B. C. Muddle, Structure and energetics of the coherent interface between the theta' precipitate phase and aluminium in Al-Cu, *Acta Mater.* 59 (2011) 7043–7050.

[43] L. Reich, S. P. Ringer, K. Hono, Origin of the initial rapid age hardening in an Al-1.7 at. % Mg-1.1 at.% Cu alloy, *Philos. Mag. Lett.* 79 (1999) 639–648.

[44] S. Ringer, T. Sakurai, I. Polmear, Origins of hardening in aged Al-Cu-Mg-(Ag) alloys, *Acta Mater.* 45 (1997) 3731–3744.

[45] A. Deschamps, B. Decreus, F. De Geuser, T. Dorin, M. Weyland, The influence of precipitation on plastic deformation of Al-Cu-Li alloys, *Acta Mater.* 61 (2013) 4010–4021.

[46] B. I. Rodgers, P. B. Prangnell, Quantification of the influence of increased pre-stretching on microstructure-strength relationships in the Al-Cu-Li alloy AA2195, *Acta Mater.* 108 (2016) 55–67.

[47] J. da Costa Teixeira, D. G. Cram, L. Bourgeois, T. J. Bastow, A. J. Hill, C. R. Hutchinson, On the strengthening response of aluminum alloys containing shear-resistant plate-shaped precipitates,

Acta Mater. 56 (2008) 6109–6122.

[48] J. F. Nie B. C. Muddle,"On the form of the age-hardening response in high strength aluminium alloys, *Mater. Sci. Eng. A* 319–321 (2001) 448–451.

[49] R. Goswami, N. Bernstein, Effect of interfaces of grain boundary Al2CuLi plates on fracture behavior of Al-3Cu-2Li, *Acta Mater.* 87 (2015) 399–410.

[50] F. De Geuser, B. Malard, A. Deschamps, Microstructure mapping of a friction stir welded AA2050 Al–Li–Cu in the T8 state, *Phil. Mag.* 94 (2014) 1451–1462.

Figure(s)

Alloys	Cu	Li	Mg	Ag	Zn
Base	3.5	0.9			
Base + 0.3Ag	3.5	0.9		0.35	
Base + Mg	3.5	0.9	0.35		
Base + Mg0.1Ag	3.5	0.9	0.35	0.11	
Base + Mg0.3Ag	3.5	0.9	0.35	0.35	
Base + MgZn	3.5	0.9	0.35		0.6
Base + Mg0.1AgZn	3.5	0.9	0.35	0.11	0.6

Table 1: Alloy compositions (all in wt%)

Alloys	Aging time	Maximum hardness	Average T_1 diameter [nm]
Base	50	148	42
Base + 0.3Ag	50	154	43
Base + Mg	20	162	45
Base + Mg0.1Ag	18	170	60
Base + Mg0.3Ag	18	173	45
Base + MgZn	18	170	48
Base + Mg0.1AgZn	15	174	55

Table 2: Ageing times to reach the 'stabilized' condition in all investigated alloys, and corresponding hardness and average diameter of T_1 precipitates measured from conventional TEM dark field images such as those presented in Figure 2.

Alloys	**Calculated area from DSC [J/g]**	**Volume fraction [%]**
Base + Mg	17.73	3.31
Base + Mg0.1Ag	20.45	3.77
Base + Mg0.3Ag	21.94	4.04
Base + MgZn	21.73	4.00
Base + Mg0.1AgZn	23.62	4.35

Table 3 : Calculated area below the DSC curve in J/g and corresponding T_1 volume fraction, by using the relationship from [24], in the different Mg-containing alloys.

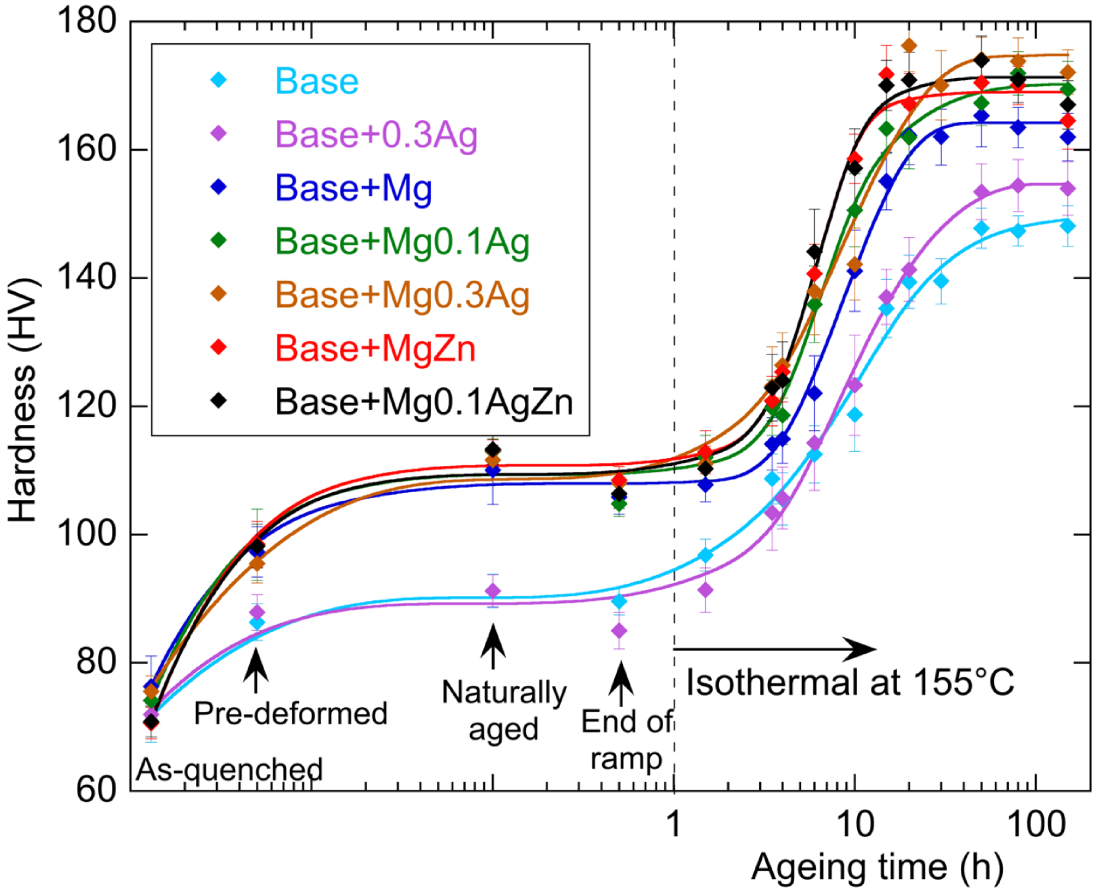

Figure 1: Effect of Mg, Ag and Zn additions on hardness evolution during 155°C isothermal ageing.

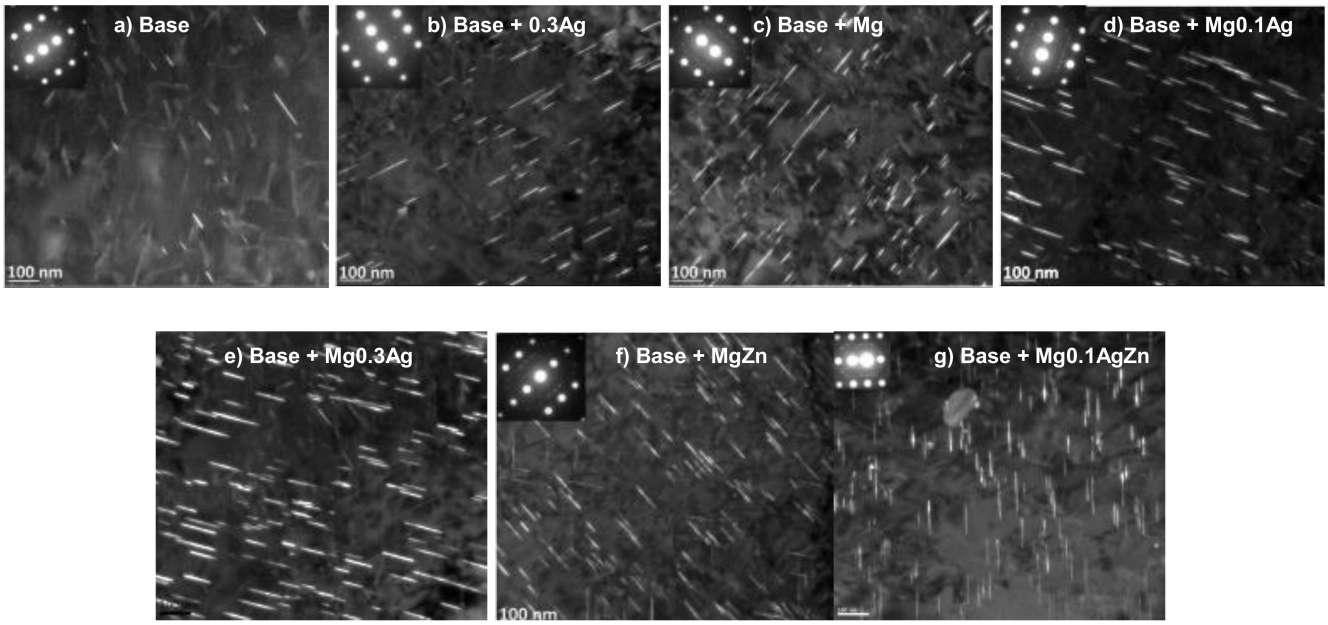

Figure 2: Dark field TEM images for all alloys illustrate the effect of Mg, Ag and Zn on the distribution of T_1 precipitates in the stabilized condition. All TEM pictures are taken with same magnification, in <112> zone axis. Histograms built from measurements on dark field images of the projected length of T_1 precipitates can be found in supplementary material. Images b) and g) are taken from [16].

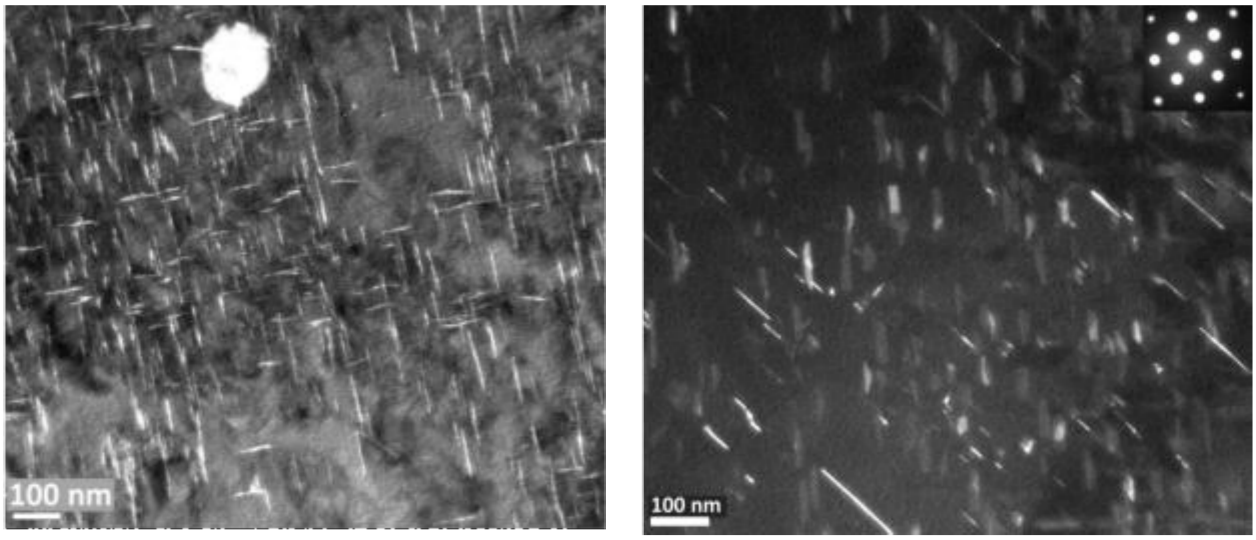

(a) (b)

Figure 3 : Dark field images in <001> zone axis of (a) Base alloy and (b) Base + Mg0.1Ag alloy in the stabilized condition.

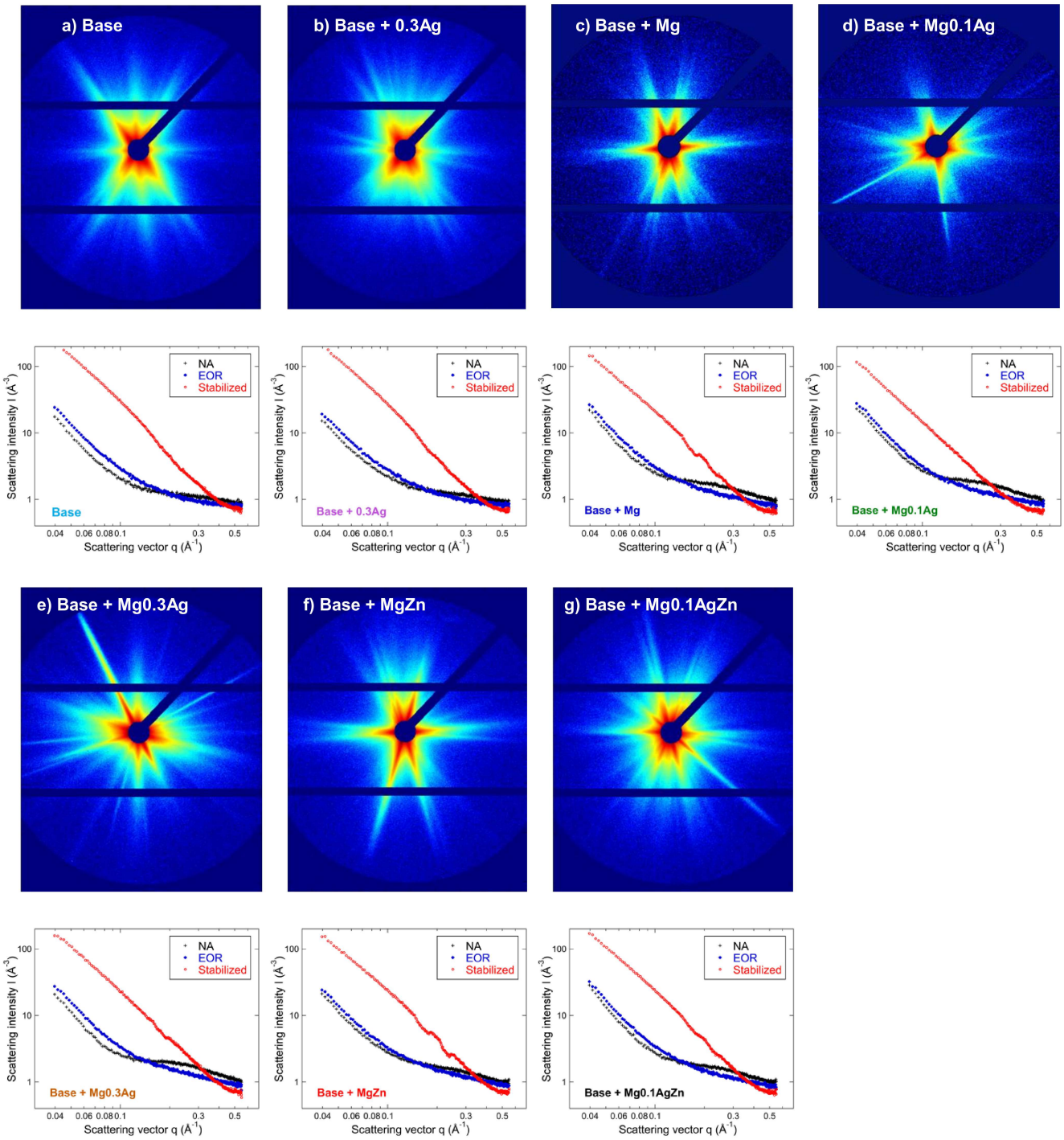

Figure 4 : SAXS images in the stabilized condition for all alloys. Below the images are shown the radially averaged I vs. q plots for 3 different aging conditions of each alloy : NA, EoR and stabilized.

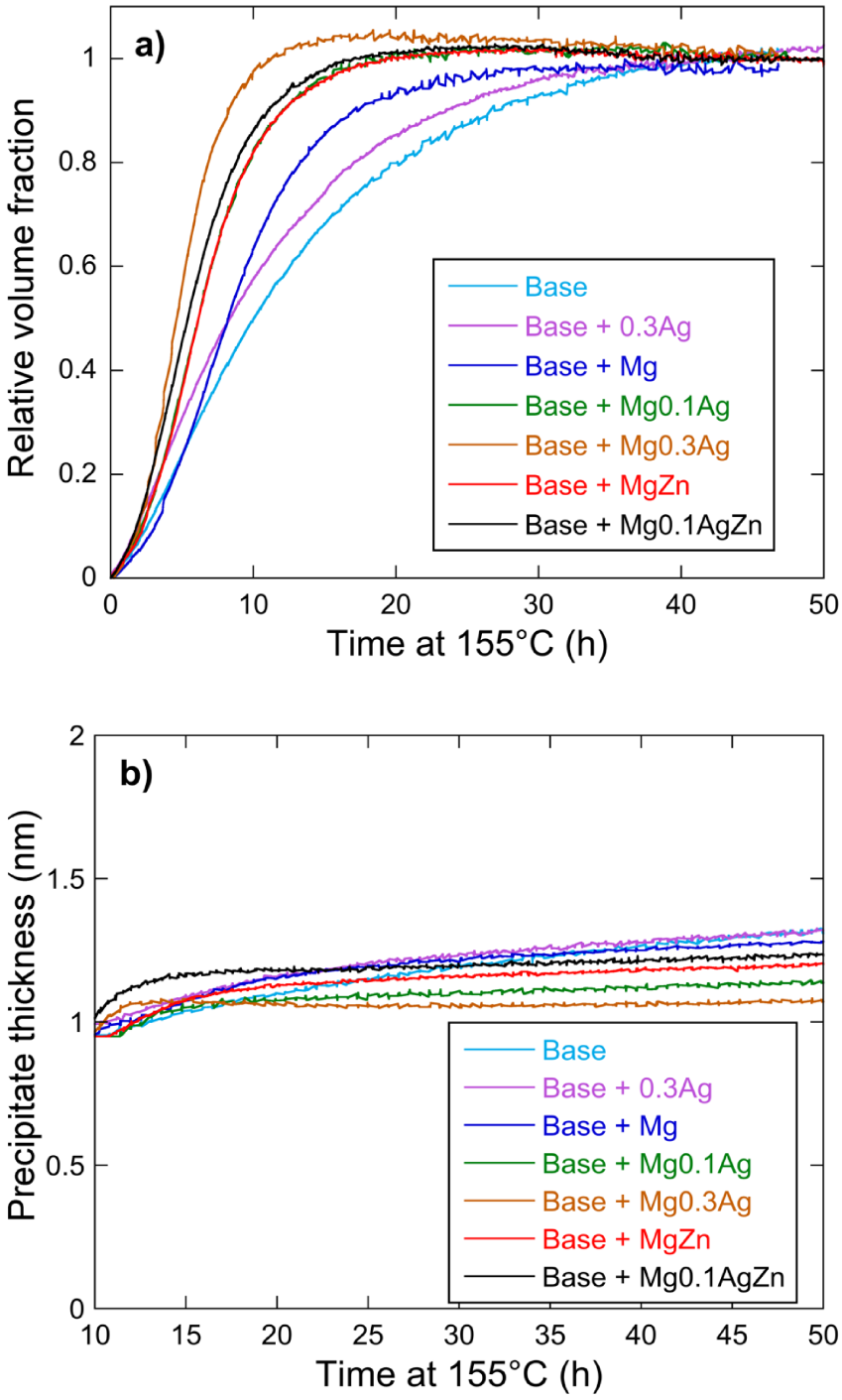

Figure 5: Evolution of a) precipitate volume fraction and (b) precipitate thickness during ageing at 155°C measured by in-situ SAXS for all alloys.

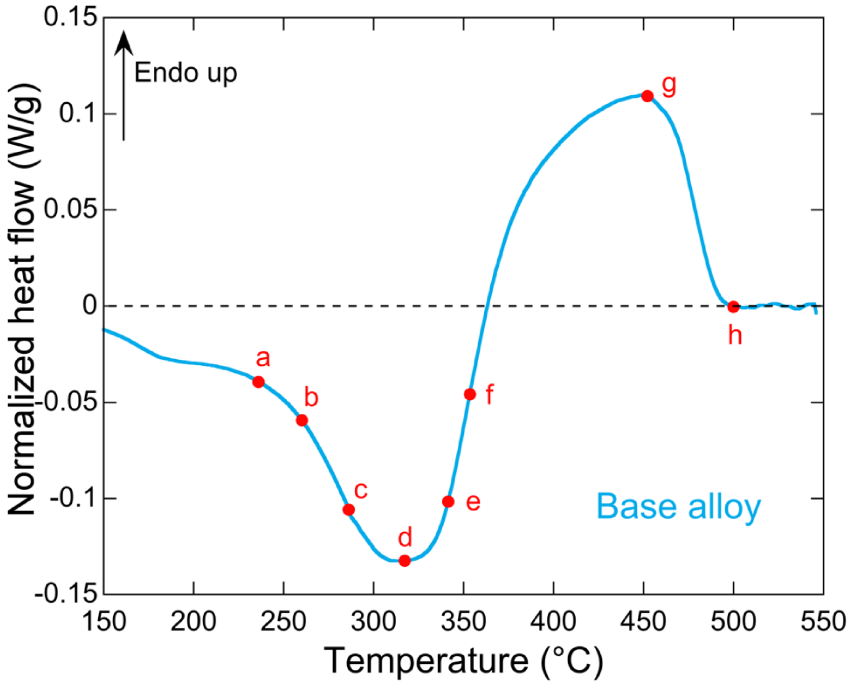

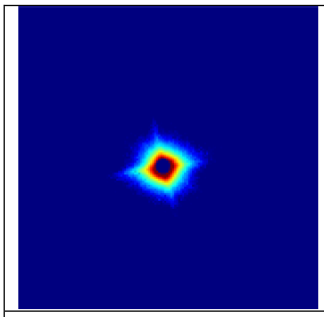	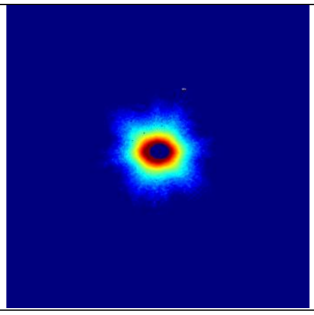	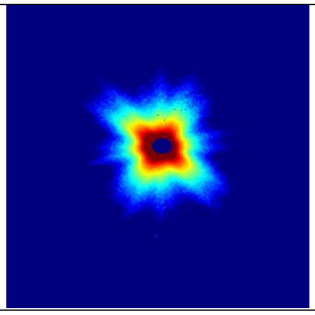	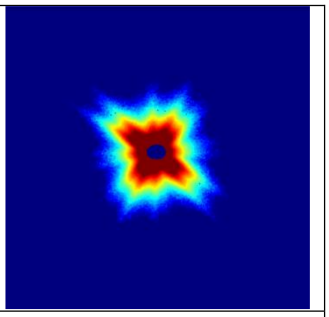
a) 236 °C	b) 260 °C	c) 286 °C	d) 317 °C
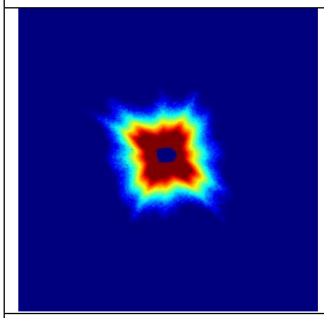	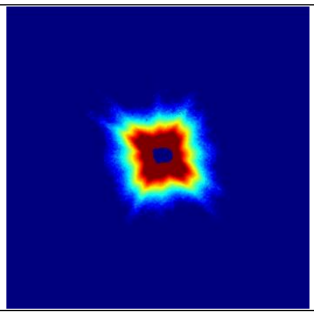	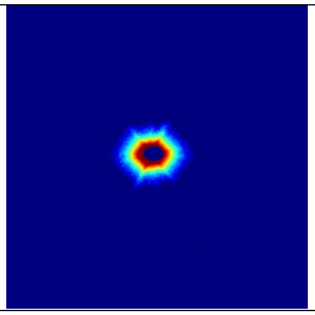	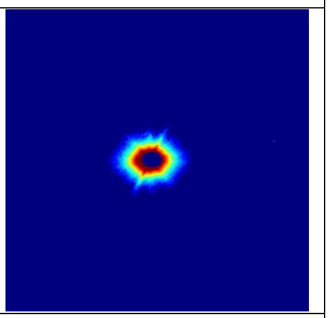
e) 341 °C	f) 353 °C	g) 452 °C	h) 500 °C

Figure 6 : DSC curve measured on the Base alloy with 50 °C/min from a naturally aged condition. (a) to (h): SAXS images at different temperatures during the ramp heating at 50 °C/min corresponding to the points indicated in the DSC curve.

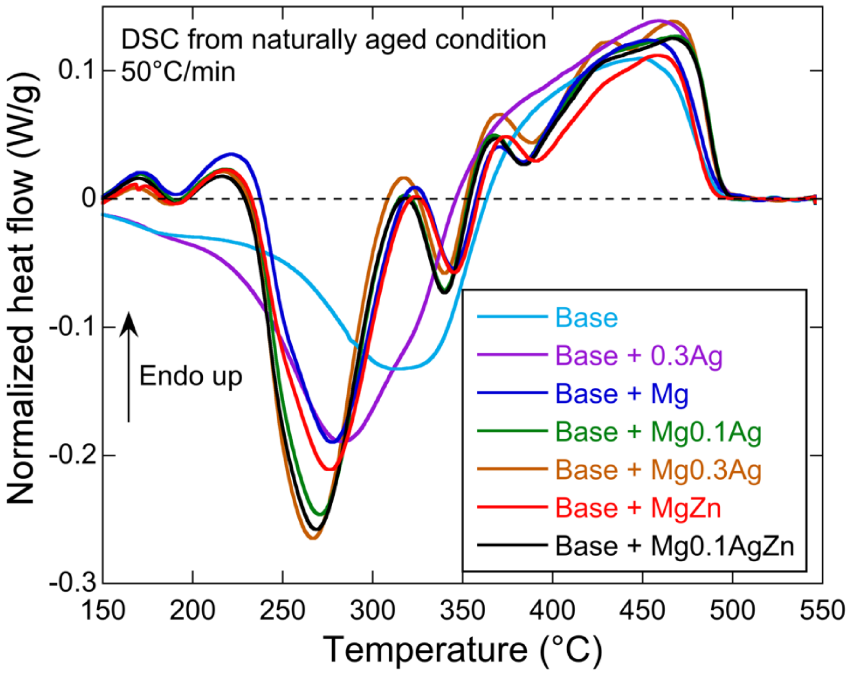

Figure 7: DSC graphs at 50 °C/min heating rate from the naturally aged (NA) state for all alloys

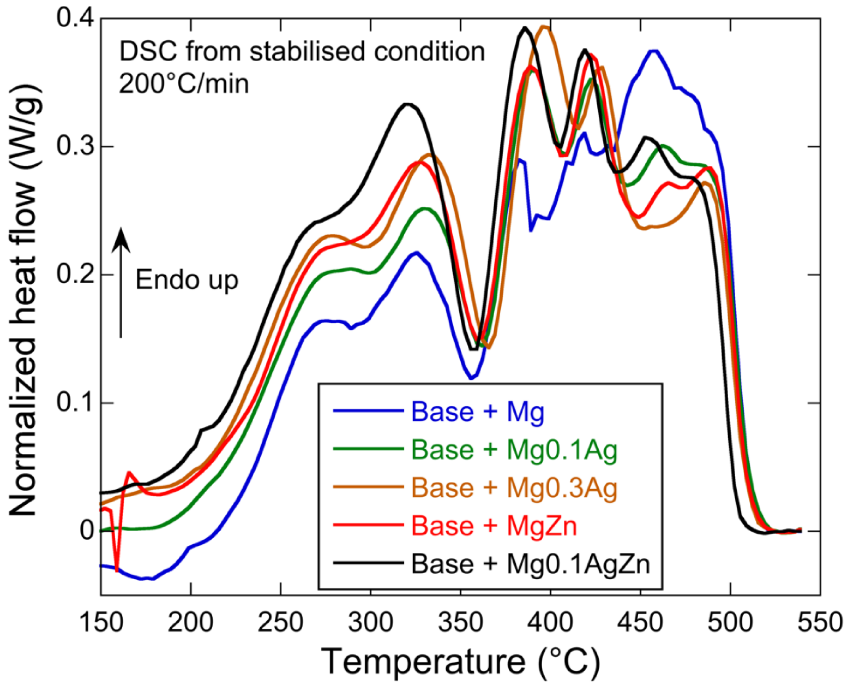

Figure 8: DSC graphs at 200 °C/min heating rate from the stabilized condition for all alloys

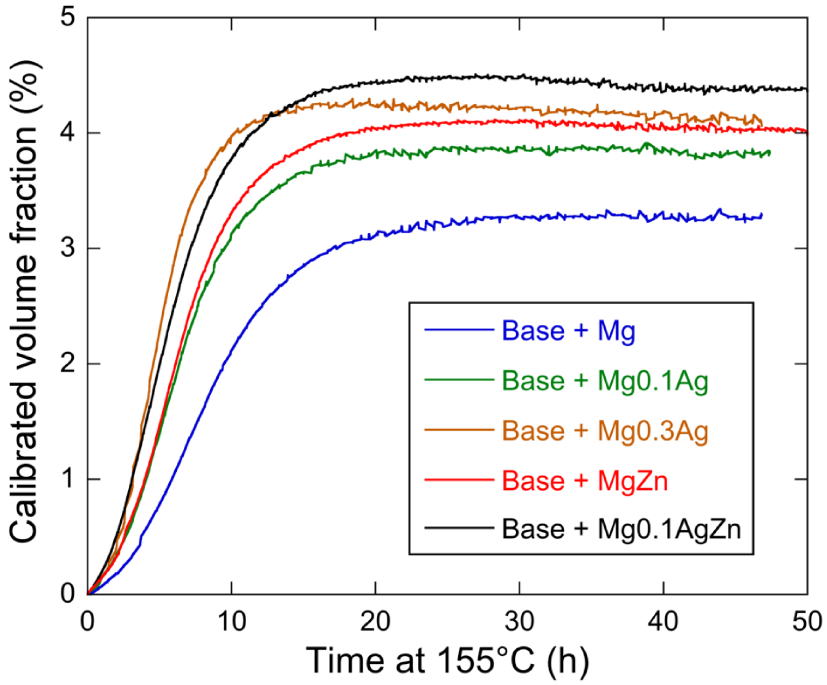

Figure 9: Evolution of calibrated volume fraction for the Mg containing alloys during ageing at 155°C.

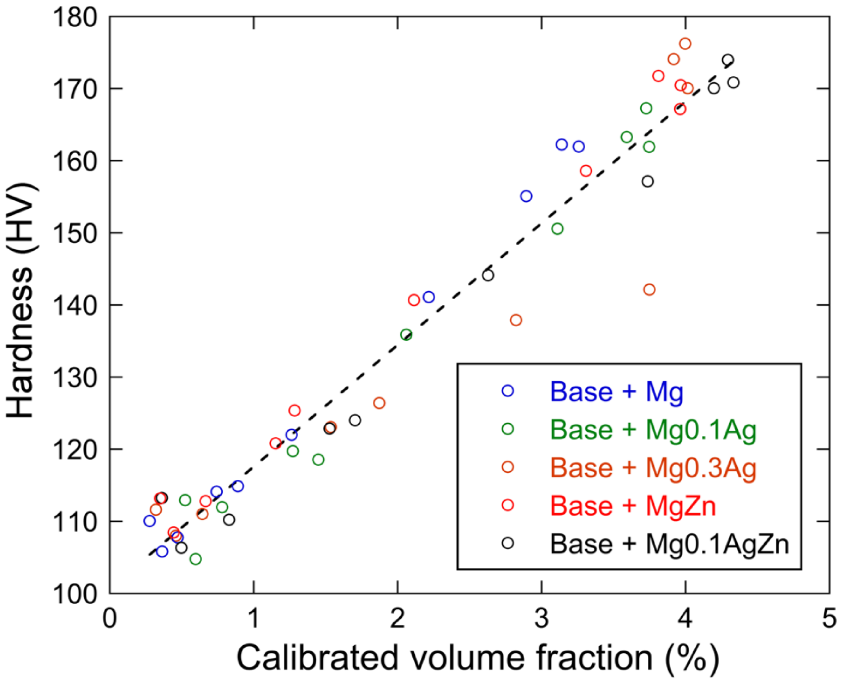

Figure 10: Variation of the hardness of the different Mg containing alloys with the calibrated volume fraction of T_1 precipitates formed during isothermal aging at 155°C.